Comparative Study of Microstructure-sensitive Fatigue Crack Propagation in Coarse- and Fine-grained Microstructures between Stable and Metastable Austenitic Stainless Steels Using Miniature Specimen

Matsushita, Aya
Department of Materials Science and Engineering, Kumamoto University

Ueki, Shohei
Department of Materials Science and Engineering, Kumamoto University

Mine, Yoji
Department of Materials Science and Engineering, Kumamoto University

Takashima, Kazuki
Department of Materials Science and Engineering, Kumamoto University

出版情報：ISIJ International. 61 (5), pp.1688-1697, 2021-05-15. 一般社団法人日本鉄鋼協会
バージョン：

ISIJ International, Vol. 61 (2021), No. 5, pp. 1688–1697
https://doi.org/10.2355/isijinternational.ISIJINT-2020-659

Comparative Study of Microstructure-sensitive Fatigue Crack Propagation in Coarse- and Fine-grained Microstructures between Stable and Metastable Austenitic Stainless Steels Using Miniature Specimen

Aya MATSUSHITA,[1)] Shohei UEKI,[2)] Yoji MINE[1)]* and Kazuki TAKASHIMA[1)]

1) Department of Materials Science and Engineering, Kumamoto University, 2-39-1 Kurokami, Chuo-ku, Kumamoto, 860-8555 Japan.
2) Department of Materials Science and Engineering, Kumamoto University. Now at Next Generation Tatara Co-Creation Centre, Organization for Industrial Innovation, Shimane University, 1060 Nishikawatsu-Cho, Matsue, Shimane, 690-8504 Japan.

(*Received on November 5, 2020; accepted on January 5, 2021; J-STAGE Advance published date: February 24, 2021*)

Microstructure-sensitive fatigue crack propagation was studied on coarse- and fine-grained stainless steels with different austenite stabilities using miniature compact-tension specimens. For coarse-grained 310S stable austenitic steel, the crack growth rate was increased by shear-localised bands formed ahead of the crack tip. For fine-grained 310S with an average grain size of ~0.25 μm, the crack-tip plastic strain was concentrated on the grains favourable to dislocation multiplication, rather than being dependent on the distance from the crack surface, which led to discontinuous crack propagation. Consequently, the fatigue crack growth rate was lower in the fine-grained 310S steel than in the coarse-grained one. In 304 metastable austenitic steel, the fatigue crack propagated within the martensite that formed ahead of the crack tip, and the crack growth rate was lower than that in the 310S steel. The grain refinement of 304 steel to a ~0.99 μm average grain size enhanced the crack growth resistance. Electron back-scatter diffraction analysis of the fracture surface revealed microstructural fragmentation due to single-variant transformation for each grain in the fine-grained 304 steel. These findings indicate that the microstructural evolution ahead of the crack tip dominates the rate of mechanically short fatigue crack propagation in austenitic stainless steels.

KEY WORDS: fatigue; stainless steels; grain size; phase transformation; plastic deformation; mechanical testing.

1. Introduction

Austenitic stainless steels are widely employed in various industries because of high resistance to corrosion and oxidation as well as excellent formability. Further weight reduction of the structure requires enhancing the low yield strength which is a major drawback of the austenitic stainless steel. The grain refinement is an effective method for strengthening, whereas it significantly decreases the ductility via the exhaustion of strain hardenability. Bimodal microstructures consisting of coarse and fine grain areas have much attention owing to good balance of the strength and ductility.[1,2)] For structural materials, fatigue properties are the most important. Fatigue crack growth tests on ultrafine-grained (UFG) low-carbon and interstitial-free steels revealed that the threshold stress intensity factor range and near-threshold fatigue crack growth resistance are lower in the UFG steels than in the coarse-grained (CG) steels.[3–5)] Kim *et al.* argued that the lower fatigue performance in the UFG steels is attributed to a reduced crack closure effect.[3)] On the other hand, Kikuchi *et al.* reported that bimodal-structured 304L stainless steel exhibits a high endurance limit compared to homogeneous CG steel and the CG structure dominates the fatigue crack propagation behaviour in the bimodal-structured steel.[6)] It is necessary to understand the fatigue process for each elementary unit cell because the bimodal microstructures are heterogeneous on the microscale where the fatigue process proceeds. Recent

* Corresponding author: E-mail: mine@msre.kumamoto-u.ac.jp

advance in the micro-mechanical testing technique enable to reveal the elementary process of fatigue crack propagation at each microstructure.[7–10)]

The resistance to fatigue crack growth is determined by intrinsic and extrinsic factors: the former arises from the deformed microstructure ahead of the crack tip, and the latter from the shielding of the crack-tip stress through the interaction in the crack wake.[11,12)] The fatigue crack growth behaviour varies considerably with the crack length.[13)] For long cracks, the growth resistance reflects the so-called crack closure phenomena[13,14)] due to the premature contact of the fracture surfaces behind the crack tip. For mechanically short crack where the small-scale yielding condition is not satisfied, the crack propagation is driven by shear deformation in addition to the reduction in the crack closure effect. The short crack propagation is sensitive to the microstructure and is strongly influenced by microstructural barriers such as grain boundaries.[15,16)] Further, the initiation and propagation of short cracks corresponding to stage I regime account for the majority of the fatigue life. Therefore, it is extremely important to quantify the intrinsic resistance to crack growth from the viewpoint of material design to improve the fatigue performance.

Low stacking fault energy materials such as stainless steels exhibit enhanced slip planarity, which results in fatigue crack propagation through strain accumulation by single shear ahead of the crack tip.[17)] In contrast, the materials favourable to cross slip, such as pure iron, have a tendency to bring about mode I opening crack growth by alternating shear.[18)] For metastable austenite such as type 304 steel, it is known that the crack closure effect due to transformation-induced plasticity enhances the extrinsic resistance to crack growth, and thereby decreases the growth rate of long cracks.[19)] The intrinsic resistance to crack growth is of significance for short cracks, but has not been revealed to date. In addition, metastable austenite is locally transformed to martensite ahead of the crack tip.[20,21)] The phase transformation complicates the damage accumulation process, which determines the crack propagation mechanism. Further, for a metastable austenitic steel, Furukane and Torizuka reported[22)] that deformation-induced martensite was formed selectively in austenite grains with a specific crystallographic orientation through grain refinement. Hence, the grain refinement of metastable austenitic steel is envisioned to considerably affect the growth rate of microstructure-sensitive cracks. This study employed miniature compact-tension (CT) specimens designed for the examination of the elementary process of microstructure-sensitive fatigue crack propagation with reduced crack closure effect, although they make a stress state different from that for microstructurally small cracks in conventional bulk specimens.[23)] The intrinsic crack growth resistance was studied using the CG and fine-grained (FG) specimens of stable austenitic stainless steel, with a focus on the mechanically short fatigue crack propagation mechanisms via the metallographic characterisation of the microstructural evolution ahead of the crack tip. The comparative study of microstructure-sensitive fatigue crack propagation in stable and metastable austenitic steels made the contribution of deformation-induced martensitic transformation and the effect of grain refinement to be revealed.

2. Materials and Methods

The materials used in this study were commercial JIS-SUS304 (304) and JIS-SUS310S (310S) steels. **Table 1** lists the chemical compositions and characteristic temperature, M_d, at which the deformation induced martensite in the steels. M_d is calculated from the chemical compositions using the Angel's equation.[24)] The 304 and 310S steels are categorised as metastable and stable austenitic steels, respectively, at room temperature. For the 304 steels, the starting materials for the CG and FG samples had different chemical compositions for the convenience of sample preparation. CG samples with an average grain size of several tens of micrometres were obtained through heat treatment at 1 403 K for 4 h, followed by water cooling. The FG samples were obtained by high-pressure torsion (HPT) processing at a rotational speed of 1 rpm for one turn under laboratory atmospheric air conditions using a disc-shaped sample with 19 mm diameter and 0.8 mm thickness. To prevent the deformation-induced martensitic transformation, the processing temperatures were set to be 473 K for 304 and 313 K for 310S, which are above the M_d temperatures (Table 1). The HPT processing was performed To reduce the density of dislocations introduced by HPT processing, FG304 and FG310S were annealed for 30 min at 973 K[25)] and 873 K,[26)] respectively. **Figure 1** illustrates the inverse pole figure maps obtained from the electron back-scatter diffraction (EBSD) analysis of the CG and FG samples of the steels. The area-weighted average grain sizes (d_{15}) of the FG304 and FG310S samples were ~0.99 and ~0.25 μm, respectively.

The heat-treated samples were thinned to ~50 μm by grinding with emery paper. The sample surface was electrochemically polished at a voltage of 40 V in an electrolyte of $HClO_4$:$C_6H_{14}O_2$:C_2H_5OH:H_2O (1:1:7:1 in volume fraction) at room temperature. The crystal orientation of the samples was determined by EBSD analysis. **Figure 2** displays the micrograph of the miniature CT specimen 0.05 mm thick and 1 mm wide fabricated using a laser beam. The tip of the notch was formed using a focus ion beam (FIB). In the CG specimens, the notch tip was located in a designed through-thickness grain. The notch plane and direction of CG310S were (110) and [001], respectively. To clarify the crystal orientation dependence of the fatigue crack growth rate, three CG304 specimens were prepared with different notch planes and directions: (001) [110], (110) [001], and (111) [$\bar{1}\,\bar{1}\,2$], respectively. **Figure 3** illustrates the crystallographic orientation relationships between the notch plane (NP), notch direction (ND), and close-packed (CP) planes {111} for the

Table 1. Chemical compositions of 304 and 310S steels used in this study. CG and FG denote the steels for coarse- and fine-grained samples, respectively. M_d indicates the characteristic temperature at which 50% of austenite is transformed to martensite by the 0.3 true strain.

	(mass%)							(K)
	C	Cr	Ni	Si	Mn	P	S	M_d
SUS304 (CG)	0.05	18.54	8.09	0.58	1.24	0.025	0.003	317
SUS304 (FG)	0.06	18.38	8.17	0.50	1.47	0.032	0.025	312
SUS310S	0.04	24.69	20.31	0.42	0.38	0.019	<0.001	129

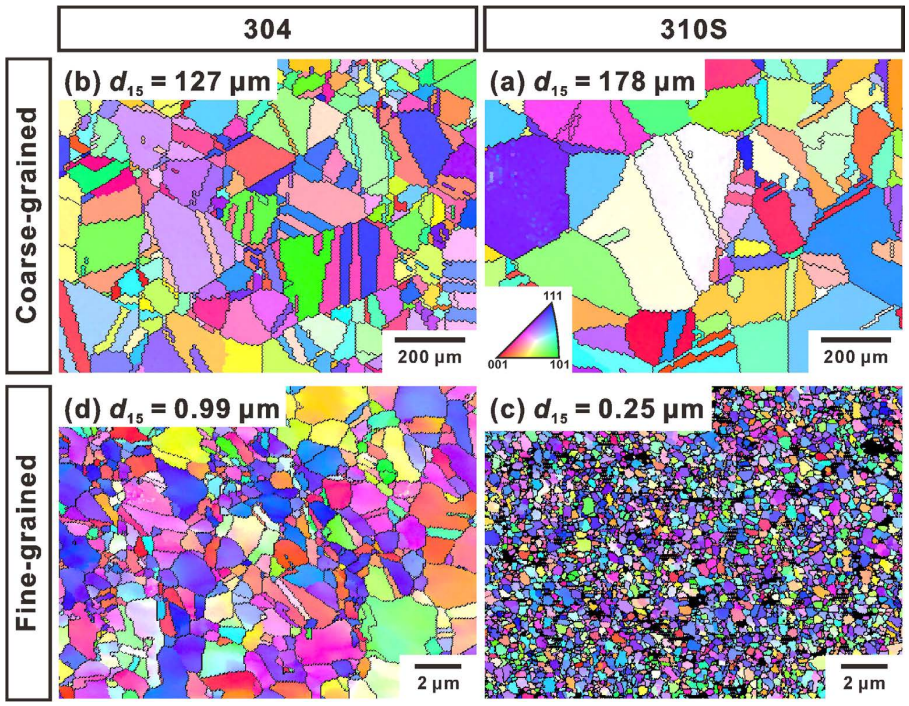

Fig. 1. EBSD inverse pole figure maps for coarse- and fine-grained 304 and 310S steels. Black lines indicate the high-angle grain boundaries with misorientation angles higher than 15°. d_{15} represents the average grain size divided by the high-angle grain boundaries. (Online version in color.)

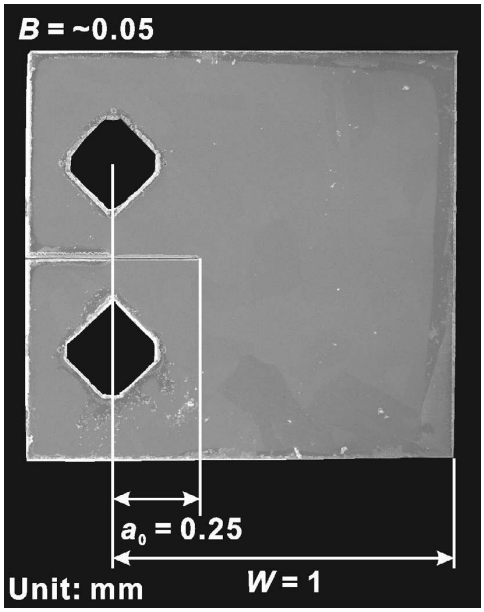

Fig. 2. SEM image of the miniature CT specimen. a_0 represents the initial notch length, W the width and B the thickness.

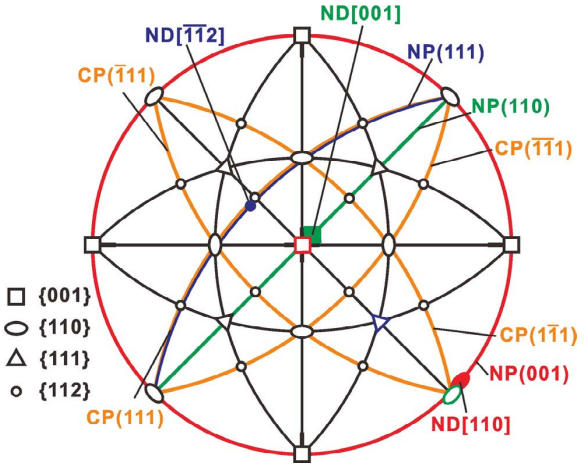

Fig. 3. Stereographic projection demonstrating the crystallographic orientation relationships between the notch plane (NP), notch direction (ND) and close-packed planes (CP) of the CG304 specimens, which are marked by red for (001) [110], by green for (110) [001], and by blue for (111) [$\bar{1}$ $\bar{1}$ 2]. (Online version in color.)

CG304 specimens. The misorientations between the real and designed notch directions were within ~8° with respect to the normal to the notch plane as the axis of rotation. The FG specimens were fabricated such that the loading and notch directions were the circumferential and radial directions of the HPT disc, respectively. Fatigue crack growth tests were performed at room temperature in laboratory atmospheric air. Cyclic loading was performed at a load ratio of 0.1 and a cyclic frequency of 1 Hz. For CG310S, a load ratio of 0.4 was also used. The crack length was measured at a predetermined number of cycles using an optical microscope to calculate the crack growth rate (da/dN). The applied stress intensity factor range (ΔK) for the CT specimen is given by the following equations:

$$\Delta K = \frac{\Delta P}{B\sqrt{W}} F\left(\frac{a}{W}\right), \quad \text{..... (1)}$$

$$F\left(\frac{a}{W}\right) = \frac{2+\frac{a}{W}}{\left(1-\frac{a}{W}\right)^{\frac{3}{2}}}\left[0.886+4.64\left(\frac{a}{W}\right)-13.32\left(\frac{a}{W}\right)^2+14.72\left(\frac{a}{W}\right)^3-5.6\left(\frac{a}{W}\right)^4\right], \quad \text{..... (2)}$$

where a represents the projected crack length, W and B are the width and thickness of the CT specimen, respectively, and ΔP is the cyclic load range.

After fatigue testing of some specimens, thin foil samples were fabricated from the crack-tip regions using FIB milling such that the foil plane was parallel to the CT specimen surface. Transmission electron microscopy (TEM) was performed at an accelerating voltage of 200 kV using electron microscopes (JEOL JEM-2100PLUS and FEI Company Tecnai F20). The thin foil sample of FG304 was analysed using transmission EBSD operating in an automatic beam scanning mode with a step size of 0.05 μm at an accelerating voltage of 30 kV. Martensite variants were determined using the TexSEM Laboratories software OIM v.7.1.0. The three-dimensional geometry of the fatigue surfaces was analysed using scanning electron microscopy (SEM) images taken with a tilt of ±5° using Alicona Imaging MeX 5.1 software. The fatigue surfaces of the 304 steel specimens were examined with EBSD operating in an automatic beam scanning mode with a step size of 0.05 μm at an accelerating voltage of 15 kV.

3. Results

3.1. Fatigue Crack Growth Properties

Figure 4 illustrates the relationships between da/dN and ΔK for the CG and FG specimens of the 310S and 304 steels. The planar dimensions of the miniature CT specimen were scaled down to a few percent with respect to a typical CT specimen, and the thickness was ~50 μm. In particular, the CG specimens had a through-thickness grain at the notch tip, which might exhibit mechanically short fatigue crack growth features. At a given ΔK, the fatigue crack growth rate was slightly lower at R = 0.1 than at R = 0.4, and it fluctuated significantly (Fig. 4(a)). The load ratio effect was sufficiently smaller than the fluctuation of the crack growth rate, which indicates that the crack closure effect[13,14] is not significantly reflected in the fatigue crack growth behaviour in the miniature CT specimen. Similarly, for FG310S (d_{15} = 0.25 μm), the crack growth rate fluctuated in the low ΔK region, whereas the da/dN–ΔK relationship exhibited stable crack growth as the ΔK level increased. At a given ΔK, the crack growth rate of the FG specimen tended to be lower than that of the CG specimen. In CG304, the fatigue crack growth rate did not depend on the crystal orientation, and it fluctuated significantly (Fig. 4(b)). When compared to those of the 310S steel (Fig. 4(a)), the 304 steel has a low crack growth rate and a great degree of improvement in the crack growth resistance owing to grain refinement (Fig. 4(b)).

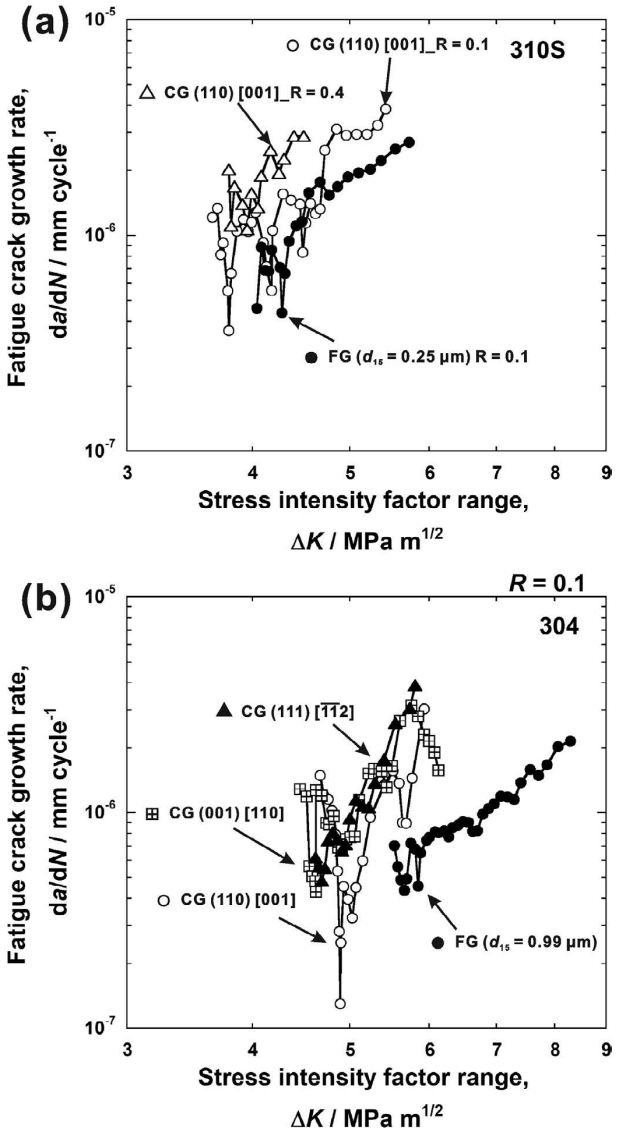

Fig. 4. Fatigue crack growth resistance curves obtained using the miniature CT specimens.

3.2. Crack Propagation and Microstructural Evolution in the 310S Steel

Figure 5 displays the crack profile, growth rate as a function of the crack length, and differential interference optical microscopy image of slip bands ahead of the crack propagating in the (110) [001]-notched CG310S specimen at R = 0.1. Coarse traces at a right angle and fine traces at approximately ±35° with respect to the notch direction are visible near the crack path (Fig. 5(a)). The coarse traces appeared prior to the crack extension and corresponded to the ($\bar{1}\,1\,\bar{1}$) or ($\bar{1}\,11$) slip. Further, the symmetric and asymmetric formation of the fine traces, which correspond to the ($\bar{1}\,\bar{1}\,1$) and (111) slips, were concurrent with the crack propagation. By focussing on the relationship between the crack profile and growth rate, it was revealed that the crack deflected from the mode I direction during the acceleration period, whereas the crack propagation direction was changed to the mode I direction during the retardation period (Fig. 5(a)). The crack growth began to decelerate and simultaneously, a slip band appeared ahead of the crack tip, as shown in Fig. 5(b) (marked by the arrows). Subsequently, when the crack began to propagate along the slip band (Fig. 5(c)), the crack growth was accelerated. At points of crack growth retardation, a shear-strain-localized region was presumably formed ahead of the crack tip while the crack was growing in the opening mode, which induced the subsequent crack-growth acceleration due to strain accumulation. The crack propagation decelerated again when the crack was out of the shear-strain localised region. The above-mentioned process was repeated throughout the crack propagation.

Figure 6 displays the fractographic images of CG310S. Overall, the fractographic observation illustrates a couple of inclined planes (regions I and II) with ridges in the direction

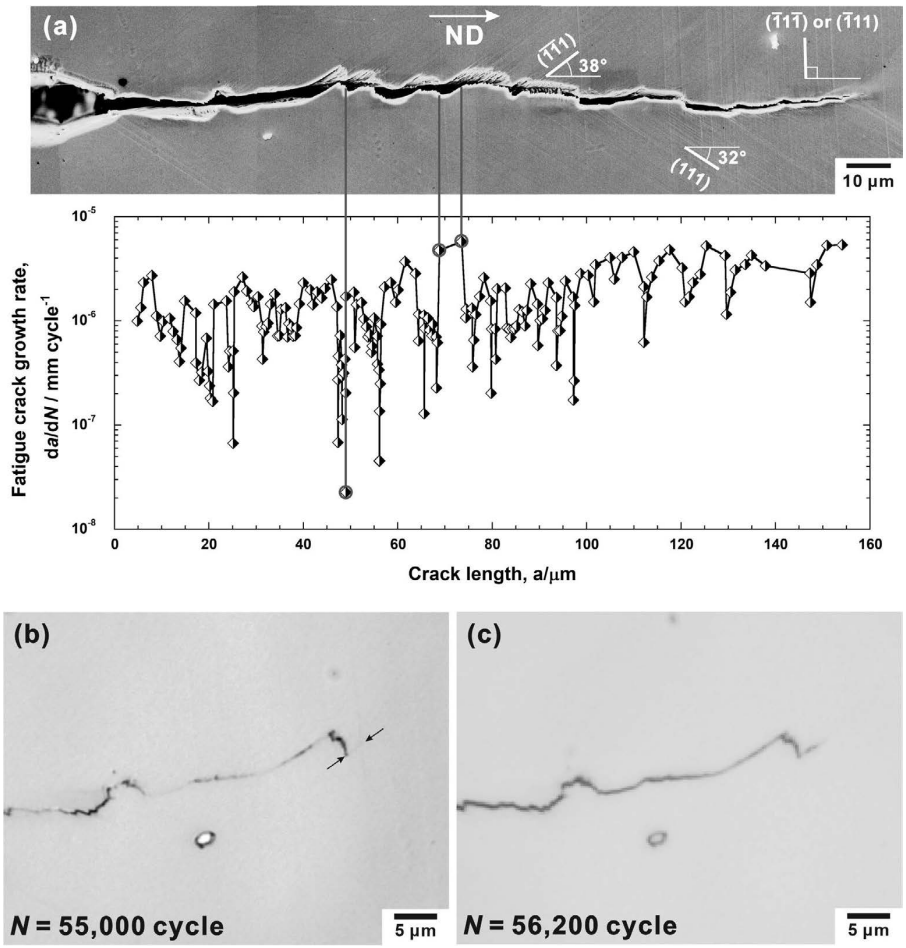

Fig. 5. (a) SEM image of crack profile and the corresponding crack growth rate in (110) [001]-notched CG310S. Optical microscopy images of (b) slip bands at crack growth retardation (differential interference contrast image) and (c) crack growing along the slip band at crack growth acceleration.

close to the crack propagation direction (Fig. 6(a)). Linear markings are visible in two directions in region I and in one direction in region II (Figs. 6(b) and 6(c)). In region I, the linear markings parallel to the z-axis correspond to the $(\bar{1}\,\bar{1}\,1)$ or $(\bar{1}\,\bar{1}\,\bar{1})$ slip and those inclined at approximately –35° with respect to the x-axis correspond to the $(\bar{1}\,11)$ slip. In contrast, region II had single-directional linear markings inclined at approximately 35° with respect to the x-axis, which corresponds to the $(\bar{1}\,1\,\bar{1})$ slip. Meanwhile, the fraction of region II was low at crack retardation (Fig. 6(d)), whereas it was high at crack acceleration (Fig. 6(e)). Therefore, the formation of region II dominates the crack-growth acceleration mechanism.

Figure 7 displays a typical fracture surface morphology in FG310S. The fatigue surface of FG310S is macroscopically flat (Fig. 7(a)), whereas microscopic bumps are visible corresponding to grains (Fig. 7(b)). In addition, ill-defined crack-arrest markings lie across multiple grains in the direction perpendicular to the crack growth direction (Fig. 7(b)).

Figure 8 illustrates the TEM bright-field image of the crack path in FG310S. Grain not only with a high density of dislocations but also with a low density were observed around the crack path (Fig. 8(a)). The distribution of the grains with a high density of dislocations was independent of the distance from the crack surface (Figs. 8(a) and 8(b)). In contrast, a low density of dislocations were observed in some grains underneath the crack surface (Figs. 8(a) and 8(c)). This suggests that the grains unfavourable to dislocation gliding rarely contribute to the crack-tip stress accommodation. Therefore, shear strain concentrates to the grains bearing plastic accommodation, which induces premature crack growth.

In addition, as shown in region D in Fig. 8(a), the crack-bridging ligaments were left behind in the crack wake. By focussing on the grain with a ligament, a high density of dislocations is visible in the bright-field image taken using $g = \bar{2}00$ (Fig. 8(d)). In contrast, most dislocations are out of contrast for $g = \bar{2}\,\bar{2}\,0$ (Fig. 8(e)); therefore, these dislocations have a Burgers vector of $(1/2)\,[1\,\bar{1}\,0]$. By considering that the resolved shear stress for the slip system due to the applied external stress is low, it is hypothesised that shear-strain localisation in the remaining grains is caused by the interaction between the cracks generated in the grains that are favourable to dislocation gliding, which results in discontinuous crack growth.

3.3. Crack Propagation and Microstructural Evolution in the 304 Steel

Figure 9 displays the crystallographic orientation relationship between the austenite matrix and formed martensite based on EBSD analysis and the TEM bright-field images obtained from the crack tip region in the (001) [110]-notched CG304 specimen. The martensite variant was formed with the habit plane parallel to $(1\,\bar{1}\,1)$ and $[10\,\bar{1}]$, which had

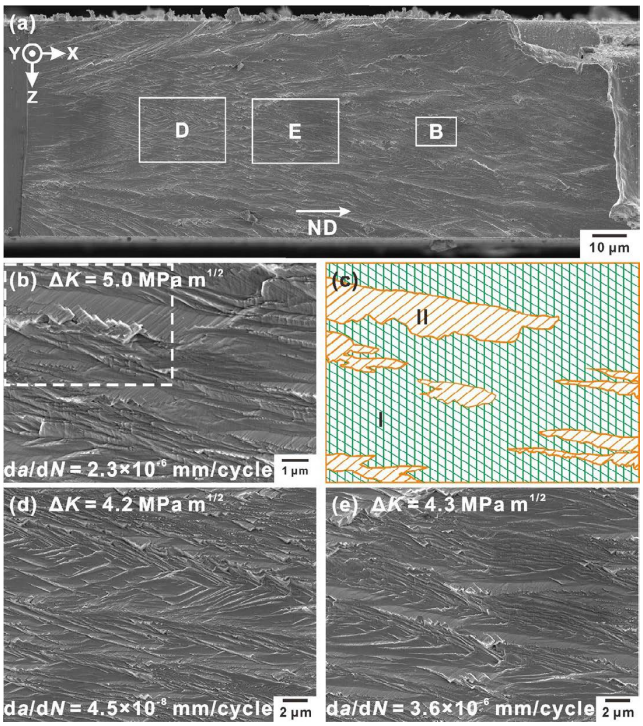

Fig. 6. (a) SEM image of overall fatigue surface in (110) [001]-notched CG310S. (b, d, and e) Magnified images of the boxed areas B, D, and E in (a), respectively. (c) Schematic illustrating the fractographic features corresponding to (b). The directions of lines indicate those of linear markings on the fracture surfaces of regions I and II. (Online version in color.)

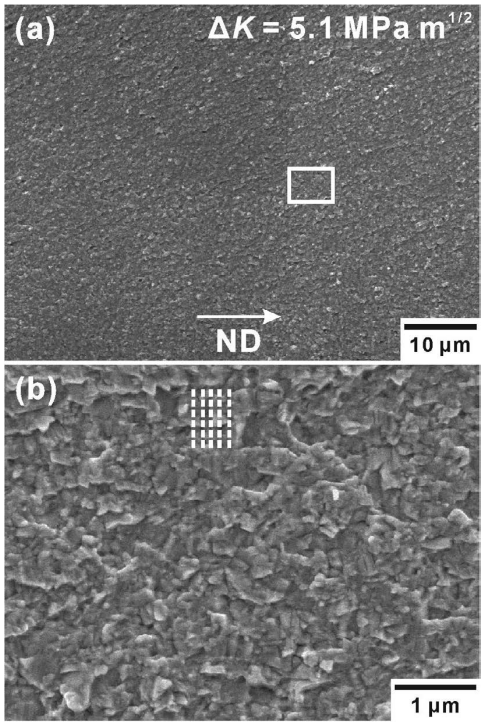

Fig. 7. (a) SEM image of the typical fractographic feature in FG310S and (b) magnified image of the boxed area in (a).

the highest shear-stress in the austenite matrix (Fig. 9(a)). Similarly, in the other CG specimens with different loading axes, the martensite variants were preferentially formed with a highly shear-stressed habit plane. This tendency is consistent with the variant selection of the deformation-induced

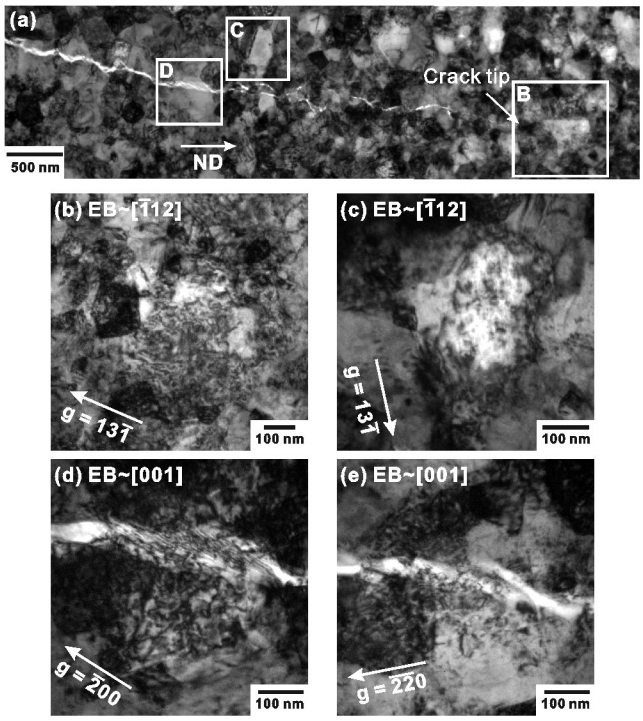

Fig. 8. (a) TEM bright-field images around the fatigue crack in FG310S: (b and c) magnified images of the boxed areas B and C, and (d and e) magnified images of the boxed area D taken using different *g*-vectors.

martensite in single crystals under monotonic loading performed by Kato and Mori.[27]

The selected-area electron diffraction patterns taken at the regions ahead of and behind the crack tip (regions I and II, respectively) display an identical martensite variant with a slight azimuth rotation (Fig. 9(b)). This indicates that the crack propagated in the martensite formed ahead of the crack tip. In addition, the bright-field image obtained using $g = \bar{2}\,\bar{2}\,0$ displays a tangle of dislocations around the crack tip (Fig. 9(b)). These dislocations have a Burgers vector of either (1/2)[111] or (1/2)[$\bar{1}\,\bar{1}\,1$]. Similarly, the bright-field images taken using $g = \bar{2}0\bar{2}$ (Fig. 9(c)) and $0\bar{2}1$ (Fig. 9(d)) display a tangle of dislocations with a Burgers vector of (1/2)[$\bar{1}\,\bar{1}\,1$] or (1/2)[$\bar{1}\,11$] and (1/2)[$\bar{1}\,\bar{1}\,1$] or (1/2)[111], respectively. Therefore, in the CG304 specimen, the crack propagated in the formed martensite via the activation of dislocations with multiple Burgers vectors, which suggests that mode I opens crack propagation.

Figure 10 illustrates the SEM images and EBSD inverse pole figure maps of the typical fatigue surface morphology in (110) [001]-notched CG304. Lath-shaped facets constituted the fatigue surface in the CG304 specimen (Fig. 10(a)). A limited number of martensite variants were observed underneath the fatigue surface (Fig. 10(b)). The crystal orientation correspondence of martensite with austenite in the (110) [001]-notched specimen reveals that similar to the (001) [110]-notched specimen, the martensite variants were formed with the habit plane that was the highest shear-stressed CP plane (Fig. 10(c)). Consequently, the martensite region spread with the (001) plane close to the fatigue surface (Fig. 10(c)). This finding indicates that the crack propagated in the martensite variants with similar orientations that had been formed ahead of the crack tip.

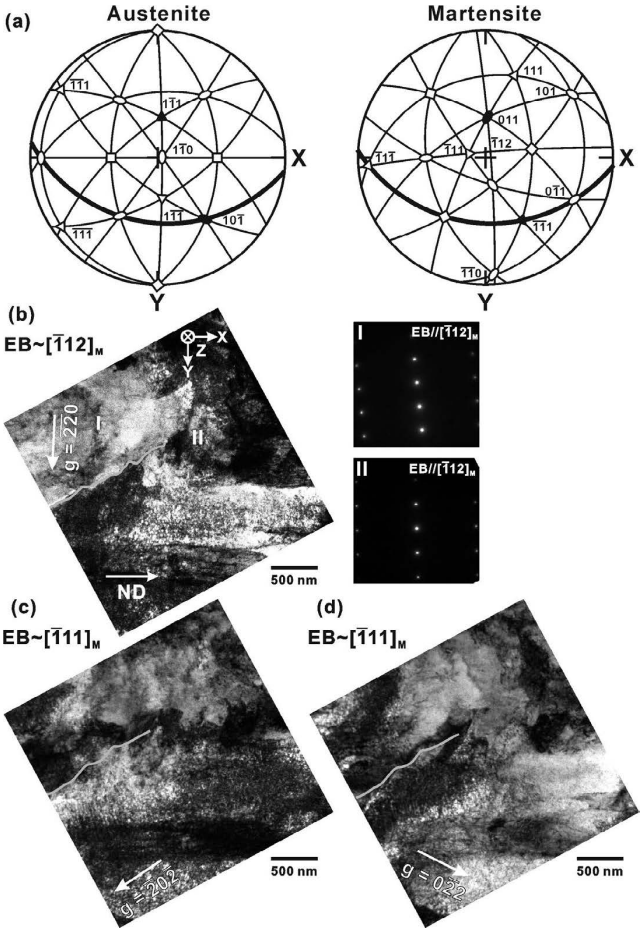

Fig. 9. (a) Stereographic projection displaying the relationship between the austenite matrix and formed martensite. (b, c, and d) TEM bright-field images of the crack-tip deformation microstructure taken using different *g*-vectors in (001) [110]-notched CG304. The selected-area electron diffraction patterns were recorded in regions I and II in (b).

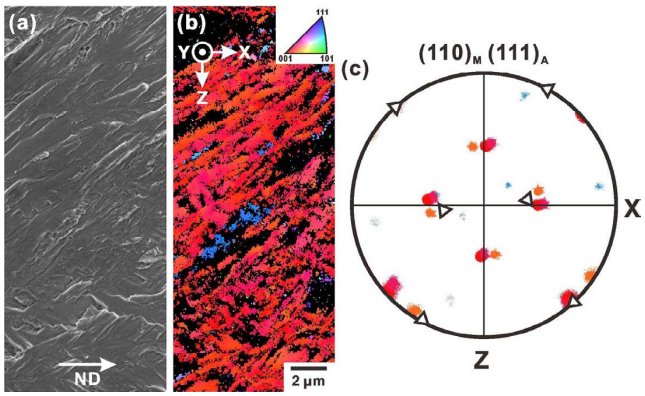

Fig. 10. (a) SEM image, (b) EBSD inverse pole figure map, and (c) corresponding $(110)_M$ and $(111)_A$ pole figure of the typical fracture surface in (110) [001]-notched CG304. (Online version in color.)

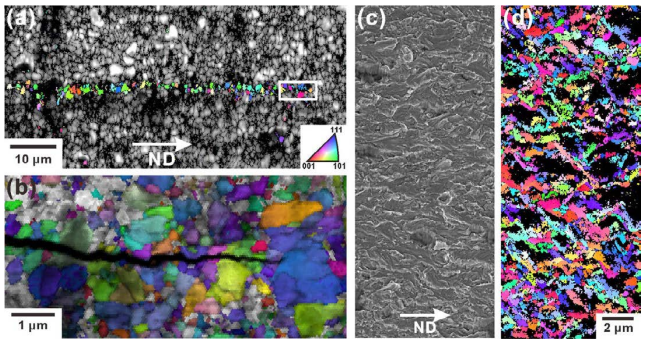

Fig. 11. (a) EBSD and (b) t-EBSD inverse pole figure maps around the crack tip. (c) SEM image and (d) EBSD inverse pole figure maps of the typical fracture surface in FG304. (Online version in color.)

Figure 11 illustrates the conventional and transmission EBSD images around the crack tip and on the fracture surface in FG304. The colour codes are based on the crystallographic orientation of martensite. Martensite was formed in a narrow region in the crack wake (Fig. 11(a)). Many martensite variants were formed with the same orientation on both sides of the crack (Fig. 11(b)). Therefore, the crack propagated in the martensite that had been formed ahead of the crack tip in both FG304 and CG304. The fracture facet sizes corresponded to the grain sizes (Fig. 11(c)), and martensite variants were observed underneath the fracture surface (Fig. 11(d)). Consequently, the formation of martensite ahead of the crack tip was confirmed in all the 304 steel specimens, while the degree of transformation and variant selection depended on the loading direction and grain size.

4. Discussion

4.1. Crack Propagation Mechanism in Stable Austenitic Steel and Grain Refinement Effect

In the CG310S stable austenitic steel, the crack-growth acceleration and retardation were repeated. The fracture surface at crack retardation had two-directional linear markings (region I), whereas the fracture surface at crack acceleration was covered with unidirectional linear markings (region II). **Figure 12** illustrates the bird's-eye view of the fracture surface constructed by 3D-SEM analysis and the stereographic projection and schematics illustrating the relationship between the fracture surface and slip planes in (110) [001]-notched CG310S. The fracture surface planes in regions I and II are different from one another, as shown in Fig. 12(a). In region I, the fracture plane is nearly parallel to (010) and coincides with the bisector of the $(\bar{1}\,11)$ and $(\bar{1}\,\bar{1}\,1)$ slip planes that can make two-directional linear markings (Fig. 12(b)). Assuming an isotropic elastic medium with a mode I crack,[28,29] $(\bar{1}\,11)$ $[0\bar{1}\,1]$ and $(\bar{1}\,\bar{1}\,1)$ [011] are the first and second highest resolved shear stress slip systems, respectively. These results suggest that dislocations having Burgers vectors of $(1/2)[0\bar{1}\,1]$ and $(1/2)$ [011] were alternately activated on the $(\bar{1}\,11)$ and $(\bar{1}\,\bar{1}\,1)$ planes, respectively, leading to mode I opening crack propagation (Fig. 12(c)). In contrast, the plane of the fracture surface covered with the unidirectional linear markings in region II is not parallel to the $(\bar{1}\,1\,\bar{1})$ slip plane, whereas the direction of the linear markings coincides with the [011] shear direction (Fig. 12(b)). The fracture surface in region II can be formed by the activation of the $(\bar{1}\,1\,\bar{1})$ and $(\bar{1}\,\bar{1}\,1)$ slips that have a common Burgers vector $(1/2)[011]$. Thus, it is plausible that the crack propagated via damage accumulation by single shearing (Fig. 12(d)).

Figure 13 displays the stress fields around the crack tip estimated for the activated slip systems and schematic

illustrating the crack propagation process for the (110) [001]-notched CG 310S stable austenitic steel. The resolved shear stress in Figs. 13(a) and 13(b) is calculated using the following formulae:[27]

$$\sigma_x = \frac{K_I}{\sqrt{2\pi r}} \cos\frac{\theta}{2}\left(1 - \sin\frac{\theta}{2}\sin\frac{3\theta}{2}\right), \quad \text{..... (3)}$$

$$\sigma_y = \frac{K_I}{\sqrt{2\pi r}} \cos\frac{\theta}{2}\left(1 + \sin\frac{\theta}{2}\sin\frac{3\theta}{2}\right), \quad \text{..... (4)}$$

$$\tau_{xy} = \frac{K_I}{\sqrt{2\pi r}} \cos\frac{\theta}{2}\sin\frac{\theta}{2}\cos\frac{3\theta}{2}, \quad \text{..... (5)}$$

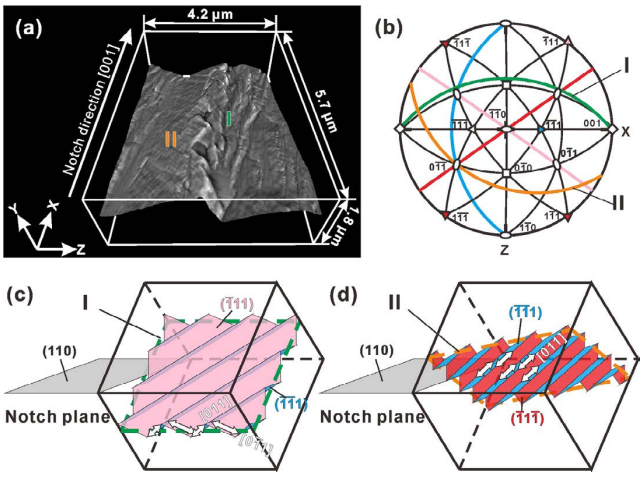

Fig. 12. (a) Bird's-eye view of the boxed area in Fig. 5(b), (b) stereographic projection and (c and d) schematics illustrating the crystallographic orientations between the fracture surfaces and available slip systems in regions I and II. (Online version in color.)

$$\sigma_z = 0, \quad \text{..... (6)}$$

where K_I represents the mode I stress intensity factor, r is the distance from the crack tip, σ_x, σ_y and σ_z, are the normal stresses on the plane perpendicular to the notch direction, notch plane, and xy plane, respectively, τ_{xy} is the shear stress on the notch plane along the notch direction, and θ is the along with respect to the notch direction on the zx plane. Slip bands are formed by the primary slip system $(\bar{1}\,11)$ $[0\,\bar{1}\,1]$ prior to the crack propagation (Fig. 13(c)), followed by the mode I opening crack propagation caused by the activation of multiple slip systems. However, a shear-strain localised region is formed ahead of the crack tip during the crack retardation period (Fig. 13(d)). Subsequently, the crack is propagated via damage accumulation by single shearing in the shear-strain localised region during the crack acceleration period (Fig. 13(e)). Malitckii *et al.*[30] measured the strain accumulation around the short fatigue cracks in a polycrystalline Fe–Cr ferritic stainless steel, which supports the crack propagation acceleration and retardation processes.

In general, the growth rate of short fatigue cracks fluctuates widely,[31] and crack growth retardation has been considered to originate from the interaction of the crack or dislocations emitted from it with the presence of grain boundaries.[32,33] However, the boundary element approach calculation by Hansson and Melin revealed[34] that the existence of large-angle grain boundaries does not significantly affect the growth rate of short fatigue cracks. Based on the experimental results, Malitckii *et al.* concluded[30] that the growth rate of short fatigue cracks is influenced by the shear-strain localised region rather than by the grain boundary. Therefore, our observation that the mechanically short fatigue cracks propagate in a through-thickness single crystal indicates that the shear-strain localised region formed

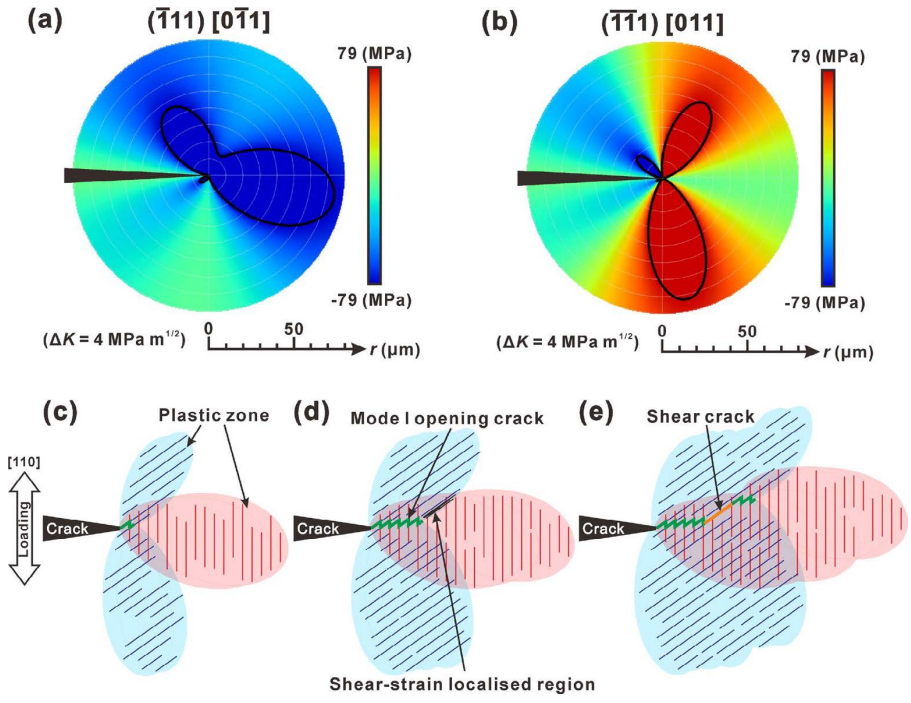

Fig. 13. (a and b) Stress fields around the crack tip estimated for the activated slip systems and schematic illustrating the fatigue crack propagation process in (110) [001]-notched CG310S. (Online version in color.)

ahead of the crack tip dominates the crack growth rates.

In summary, in CG 310S, shear-strain localised bands with a width of a few micrometres were formed ahead of the crack tip, which resulted in intermittent crack growth based on the damage accumulation process. In contrast, in FG310S, both grains favourable and unfavourable to dislocation multiplication were mixedly present in the crack wake. The same phenomenon was reported in the short fatigue crack growth of ultrafine-grained IF steel processed by accumulative roll bonding.[35] As reported in this study, the elastic stress field at the crack tip causes dislocation multiplication not only at the crack tip, but also at the grain boundaries,[36] which is presumed to result in transgranular crack growth in the grains with a high density of dislocations. Shear strain was presumably concentrated in some grains that contribute to the plastic accommodation of the crack-tip stress, and might promote crack propagation. However, the grains unfavourable to dislocation gliding hindered the continuous crack propagation, and the other grains favourable for dislocation multiplication were subjected to severe strain localisation that formed the crack-bridging ligament. It is presumed that the crack growth resistance increased as a result of adding the crack propagation process due to the damage accumulation in the crack-bridging ligament.

4.2. Crack Propagation Mechanism in Metastable Austenitic Steel and Grain Refinement Effect

The 304 metastable austenitic steel exhibited high resistance to fatigue crack growth compared to the 310S stable austenitic steel. In the CG304 specimen, the crack propagated in the martensite formed ahead of the crack tip irrespective of the loading axis. The martensite variant with the habit plane oriented to the highest shear stress plane was preferentially selected. **Figure 14** displays the schematic illustrating the crack propagation process for the (110) [001]-notched CG304 specimen. Prior to crack propagation, the first shear occurs on the $(\bar{1}\,1\,\bar{1})$ or $(\bar{1}\,11)$ plane corresponding to the primary shear system. The second shear on the $(\bar{1}\,\bar{1}\,1)$ and (111) planes, which are inclined by approximately ± 35°, respectively, with respect to the notch direction, is concurrent with the crack propagation. At the intersections of the shear bands, α' martensite is nucleated (Fig. 14(a)), as proposed by Olson and Cohen.[37] The martensite regions extend and coalesce to form a uniform martensite region ahead of the crack tip (Fig. 14(b)). This is followed by crack propagation in the martensite with almost the same crystallographic orientation, by the activation of dislocations having different Burgers vectors (Fig. 14(c)). Murr *et al.* concluded[38] that the martensite growth in CG304 steel is based on the repeated nucleation and coalescence of α' embryos at the intersections of shear bands. Therefore, for the fatigue crack growth process in CG304, the damage accumulation is delayed by the formation of martensite ahead of the crack tip when compared to CG310S. In addition, single-shear-type crack propagation is suppressed by the mode I opening crack propagation in the formed martensite. This is another reason why the crack growth resistance of CG304 was higher than that of CG310S.

For the 304 steel, the crack growth resistance was significantly enhanced by grain refinement to ~0.99 μm. Similar to CG304, in FG304, martensite was formed ahead of the crack tip, and the crack propagated within it. However, martensite variants in FG304 were formed for each grain. **Figure 15** illustrates the schematics interpreting the difference in the martensite structure formed ahead of the crack tip between the CG and FG 304 specimens. For CG304, external stress dominated the selection of martensite variants, which resulted in the formation of the martensite region having almost the same crystallographic orientation ahead of the crack tip (Fig. 15(a)). Furukane and Torizuka studied the grain size effect on the strain-induced martensitic transformation in 316L steel by liquid nitrogen temperature rolling and concluded that grain refinement restrains the progress of strain-induced martensitic transformation.[22] This suggests that the strain accumulation process was retarded via the mechanism change from intersecting shear to single variant transformation by grain refinement. In addition, the microstructural fragmentation due to the single-variant

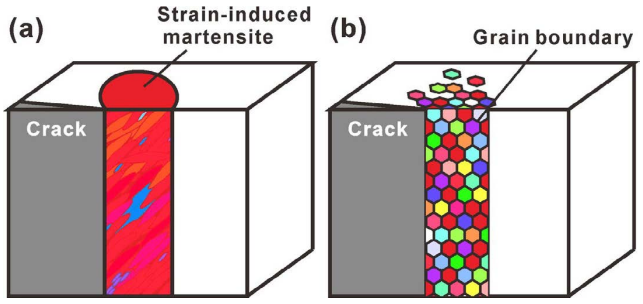

Fig. 15. Schematic illustrating the martensite variants formed ahead of the crack tip in (a) CG and (b) FG 304 steel. (Online version in color.)

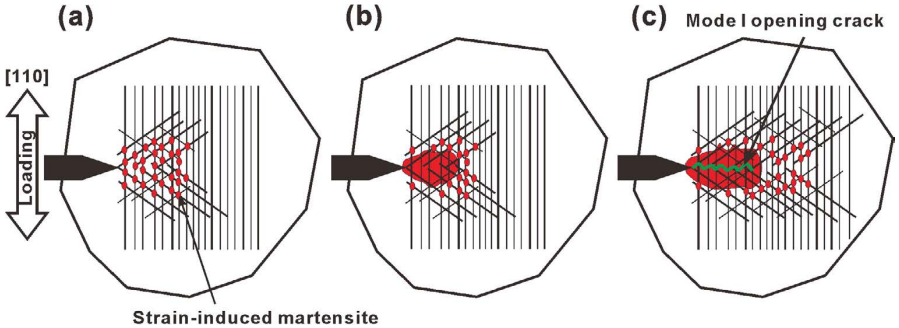

Fig. 14. Schematic illustrating the fatigue crack propagation process in (110) [001]-notched CG304. (Online version in color.)

transformation for each grain was found to enhance the crack growth resistance in the FG304 steel (Fig. 15(b)).

5. Conclusions

The elementary process of microstructure-sensitive fatigue crack growth was examined on coarse- and fine-grained (CG and FG, respectively) stainless steels with different austenite stabilities using miniature compact-tension specimens. The conclusions are summarised as follows:

(1) In the CG310S stable austenitic steel, fatigue crack growth retardation and acceleration were observed. A shear-strain localised region developed ahead of the crack tip during the retardation period. When the crack penetrated this region, the crack propagation rate accelerated. Therefore, the fatigue crack growth rate was affected by the shear localised bands formed prior to the crack propagation.

(2) For the 310S steel, the crack growth rate of the FG specimen (average grain size ~0.25 μm) was lower than that of the CG specimen. In the FG specimen, both grains favourable and unfavourable to dislocation multiplication were mixedly present in the crack wake. The transgranular cracking in the shear-strain localised region preceded the ligament bridging, which led to discontinuous crack propagation.

(3) The 304 metastable austenitic steel exhibited high resistance to crack growth compared to the 310S stable austenitic steel. The martensite variants were formed prior to crack propagation, with the degree of transformation dependent on the loading axis and grain size. It is presumed that the crack growth resistance was improved by delayed strain accumulation due to transformation and mode I opening crack propagation in the formed martensite.

(4) In the 304 steel, the crack growth resistance was increased by refining the average grain size to ~0.99 μm. Lath-shaped facets constituted the fatigue surface of the CG specimen, and a limited number of martensite variants were formed. Consequently, the crack propagated in martensite with similar crystallographic orientations. In contrast, in the FG specimen, the fracture surface facets corresponded to the grains and martensite variants with varied orientations underneath the fracture surface. It is concluded that the change in the martensite transformation mechanism and the resultant microstructural fragmentation ahead of the crack tip by grain refinement increases the crack growth resistance.

Acknowledgements

The authors thank Dr. M. Tsushida and Dr. T. Yamamuro, Kumamoto University, for their assistance in transmission EBSD and TEM studies. This study was supported in part by a Grant-in-Aid for Scientific Research (B) JP19H02464 from the Japan Society for the Promotion of Science (JSPS).

REFERENCES

1) Z. Zhang, S. K. Vajpai, D. Orlov and K. Ameyama: *Mater. Sci. Eng. A*, **598** (2014), 106. https://doi.org/10.1016/j.msea.2014.01.023
2) Z. J. Zheng, J. W. Liu and Y. Gao: *Mater. Sci. Eng. A*, **680** (2017), 426. https://doi.org/10.1016/j.msea.2016.11.004
3) H. K. Kim, M. I. Choi, C. S. Chung and D. H. Shin: *Mater. Sci. Eng. A*, **340** (2003), 243. https://doi.org/10.1016/S0921-5093(02)00178-8
4) M. D. Chapetti, H. Miyata, T. Tagawa, T. Miyata and M. Fujioka: *Int. J. Fatigue*, **27** (2005), 235. https://doi.org/10.1016/j.ijfatigue.2004.07.004
5) T. Niendorf, F. Rubitschek, H. J. Maier, D. Canadinc and I. Karaman: *J. Mater. Sci.*, **45** (2010), 4813. https:// doi.org/10.1007/s10853-010-4511-7
6) S. Kikuchi, Y. Nukui, Y. Nakatsuka, Y. Nakai, M. Nakatani, M. O. Kawabata and K. Ameyama: *Int. J. Fatigue*, **127** (2019), 222. https://doi.org/10.1016/j.ijfatigue.2019.06.016
7) S. Ueki, Y. Mine and K. Takashima: *Corros. Sci.*, **129** (2017), 205. https://doi.org/10.1016/j.corsci.2017.10.013
8) Y. Mine, S. Katashima, R. Ding, P. Bowen and K. Takashima: *Scr. Mater.*, **165** (2019), 107. https://doi.org/10.1016/j.scriptamat.2019.02.029
9) S. Ueki, T. Matsumura, Y. Mine, S. Morito and K. Takashima: *Scr. Mater.*, **173** (2019), 80. https://doi.org/10.1016/j.scriptamat.2019.08.004
10) S. Ueki, Y. Mine and K. Takashima: *Mater. Sci. Eng. A*, **773** (2020), 138830. https://doi.org/10.1016/j.msea.2019.138830
11) R. O. Ritchie: *Mater. Sci. Eng. A*, **103** (1988), 15. https://doi.org/10.1016/0025-5416(88)90547-2
12) S. Suresh: Fatigue of Materials, Cambridge University Press, Cambridge, UK, (1998), 483.
13) S. Suresh and R. O. Ritchie: *Int. Met. Rev.*, **29** (1984), 445. https://doi.org/10.1179/imtr.1984.29.1.445
14) S. Suresh and R. O. Ritchie: *Metall. Trans. A*, **13** (1982), 1627. https://doi.org/10.1007/BF02644803
15) A. Pineau, D. L. McDowell, E. P. Busso and S. D. Antolovich: *Acta Mater.*, **107** (2016), 484. https://doi.org/10.1016/j.actamat.2015.05.050
16) P. Chowdhury and H. Sehitoglu: *Fatigue Fract. Eng. Mater. Struct.*, **39** (2016), 652. https://doi.org/10.1111/ffe.12392
17) M. Gell and G. R. Leverant: *Trans. AIME*, **242** (1968), 1869.
18) F. O. Riemelmoser, R. Pippan and H. P. Stüwe: *Acta Mater.*, **46** (1998), 1793. https://doi.org/10.1016/S1359-6454(97)00366-2
19) A. G. Pineau and R. M. Pelloux: *Metall. Trans.*, **5** (1974), 1103. https://doi.org/10.1007/BF02644322
20) Z. Mei and J. W. Morris: *Metall. Trans. A*, **21** (1990), 3137. https://doi.org/10.1007/BF02647310
21) J. Stolarz, N. Baffie and T. Magnin: *Mater. Sci. Eng. A*, **319**–**321** (2001), 521. https://doi.org/10.1016/S0921-5093(01)01072-3
22) S. Furukane and S. Torizuka: *Tetsu-to-Hagané*, **105** (2019), 827 (in Japanese). https://doi.org/10.2355/tetsutohagane.TETSU-2019-004
23) J. P. Campbell and R. O. Ritchie: *Eng. Fract. Mech.*, **67** (2000), 209. https://doi.org/10.1016/S0013-7944(00)00046-1
24) T. Angel: *J. Iron Steel Inst.*, **177** (1954), 165.
25) Y. Mine, N. Horita, Z. Horita and K. Takashima: *Int. J. Hydrog. Energy*, **42** (2017), 15415. https://doi.org/10.1016/j.ijhydene.2017.04.249
26) Y. Mine, K. Tachibana and Z. Horita: *Metall. Mater. Trans. A*, **42** (2011), 1619. https://doi.org/10.1007/s11661-010-0558-y
27) M. Kato and T. Mori: *Acta Metall.*, **24** (1976), 853. https://doi.org/10.1016/0001-6160(76)90052-3
28) S. Suresh: Fatigue of Materials, Cambridge University Press, Cambridge, UK, (1998), 288.
29) Y. Mine and K. Takashima: *Mater. Sci. Eng. A*, **534** (2012), 260. https://doi.org/10.1016/j.msea.2011.11.067
30) E. Malitckii, H. Remes, P. Lehto, Y. Yagodzinskyy, S. Bossuyt and H. Hänninen: *Acta Mater.*, **144** (2018), 51. https://doi.org/10.1016/j.actamat.2017.10.038
31) D. Taylor and J. F. Knott: *Fatigue Fract. Eng. Mater. Struct.*, **4** (1981), 147. https://doi.org/10.1111/j.1460-2695.1981.tb01116.x
32) K. Tanaka, Y. Nakai and M. Yamashita: *Int. J. Fract.*, **17** (1981), 519.
33) A. Navarro and E. R. de los Rios: *Philos. Mag. A*, **57** (1988), 15. https://doi.org/10.1080/01418618808204496
34) P. Hansson and S. Melin: *Int. J. Fract.*, **165** (2010), 199. https://doi.org/10.1007/s10704-010-9512-7
35) X. Lin, M. Koyama, S. Gao, N. Tsuji, K. Tsuzaki and H. Noguchi: *Int. J. Fatigue*, **118** (2019), 117. https://doi.org/10.1016/j.ijfatigue.2018.09.002
36) T. Shimokawa, M. Tanaka, K. Kinoshita and K. Higashida: *Phys. Rev. B*, **83** (2011), 214113. https://doi.org/10.1103/PhysRevB.83.214113
37) G. B. Olson and M. Cohen: *J. Less-Common Met.*, **28** (1972), 107. https://doi.org/10.1016/0022-5088(72)90173-7
38) L. E. Murr, K. P. Staudhammer and S. S. Hecker: *Metall. Trans. A*, **13** (1982), 627. https://doi.org/10.1007/BF02644428